

# Porous Fibers Composed of Polymer Nanoball Decorated Graphene for Wearable and Highly Sensitive Strain Sensors

Tao Huang, Peng He,\* Ranran Wang, Siwei Yang, Jing Sun, Xiaoming Xie, and Guqiao Ding\*

Wearable textile strain sensors that can perceive and respond to human stimuli are an essential part of wearable electronics. Yet, the detection of subtle strains on the human body suffers from the low sensitivity of many existing sensors. Generally, the inadequate sensitivity originates from the strong structural integrity of the sensors because tiny external strains cannot trigger enough variation in the conducting network. Inspired by the rolling friction where the interaction is weakened by decreasing interface area, porous fibers made of graphene decorated with nanoballs are prepared via a prolonged phase-separation process. This novel structure confers the graphene fibers with high gauge factors (51 in 0–5% and 87 in 5–8%), which is almost 10 times larger than the same structures without nanoballs. A low detection limit (0.01% strain) and good durability (over 6000 circles) are obtained. By the virtue of these qualities, these fiber-based textile sensors can recognize a pulse wave and eyeball movement in real-time while keeping comfortable wearing sense. Moreover, by weaving such fibers, the electronic fabrics with a specially designed structure can distinguish the multilocation in real time, which shows great potential as wearable electronics.

textile strain sensors are easier to integrate into daily garments. Also, the fibers or textiles have excellent flexibility and can follow many intricate motions of the human body.<sup>[4]</sup> Besides, fibers crossed in fabrics will prevent the crack propagation that occurs in solid films or bulks, thereby improving their long-term use.<sup>[4]</sup> In addition, the textiles have a comfortable appeal and can be “breathable” or keep the subject warm.<sup>[5]</sup> Therefore, the fiber or textiles are the most suitable platform to fabricate high-performance wearable sensors. Previously, we had developed stretchable strain sensors using reduced graphene oxide (rGO) coated on double-covered yarn to detect torsion and stretching.<sup>[6]</sup> Yang et al. coated rGO onto polyester fabrics without encapsulation to make fabric-based strain sensors to detect different gestures.<sup>[7]</sup> In general, fiber or textile-based sensors possess good motion response, high flexibility, a short response-time, long-term

## 1. Introduction

Wearable sensors to monitor various human actions are considered an essential part of wearable electronics.<sup>[1,2]</sup> Compared with traditional membrane-based strain sensors,<sup>[3]</sup> fiber or


stability, and excellent durability. Nowadays, many fiber/textile sensors have been explored for their high gauge factor in the higher strain range (over 100% strain).<sup>[8–11]</sup> In fact, for human body, many vital health signals such as the pulse and breath generate less than 1% strain.<sup>[12]</sup> Therefore, it poses a challenge to the textile-based strain sensors because of the insufficient sensitivity (i.e., gauge factor:  $GF < 50$ ) compared to membrane-based sensors ( $GF > 1000$ ).<sup>[13–17]</sup>

Normally, polymer fibers or textiles are insulator, hence much progress has been made to develop conductive fabrics. Zhong et al. interpenetrated Ag nanowires into polyolefin elastomer nanofibrous yarn for low detection limit (0.065% strain) and high GF ( $>1000$  at strain over 100%), but Ag nanowires was vulnerable to oxidation.<sup>[18]</sup> Liquid metal gallium based conducting microfiber was also developed for wearable and washable sensors but with a very low gauge factor ( $GF = 1$  at 30% strain).<sup>[19]</sup> By contrast, graphene is light, flexible, electrically conducting, and has a low-Johnson-noise.<sup>[20]</sup> It presents much potential for future wearable electronics.<sup>[21–23]</sup> More importantly, graphene fibers can be woven into the fabrics for further intelligent cloth integration without any encapsulation.<sup>[22]</sup> However, normal graphene fibers have a high tensile strength around 1.45 GPa, which means that their resistance can hardly change to reflect the external strain.<sup>[23]</sup> Loosely interconnected graphene sheets mechanically bonded by polydimethylsiloxane

T. Huang, Dr. P. He, Dr. S. W. Yang, Prof. X. M. Xie, Prof. G. Q. Ding  
Center for Excellence in Superconducting Electronics (CENSE)  
State Key Laboratory of Functional Materials for Informatics  
Shanghai Institute of Microsystem and Information Technology (SIMIT)  
Chinese Academy of Sciences  
Shanghai 200050, P. R. China  
E-mail: hepeng@mail.sim.ac.cn; gqding@mail.sim.ac.cn

T. Huang, Dr. P. He, Dr. S. W. Yang, Prof. X. M. Xie, Prof. G. Q. Ding  
College of Materials Science and Opto-Electronic Technology  
University of Chinese Academy of Sciences  
Beijing 100049, P. R. China

Dr. R. R. Wang, Prof. J. Sun  
State Key Laboratory of High Performance Ceramics  
and Superfine Microstructure  
Shanghai Institute of Ceramics  
Chinese Academy of Sciences  
Shanghai 200050, China

 The ORCID identification number(s) for the author(s) of this article can be found under <https://doi.org/10.1002/adfm.201903732>.

DOI: 10.1002/adfm.201903732

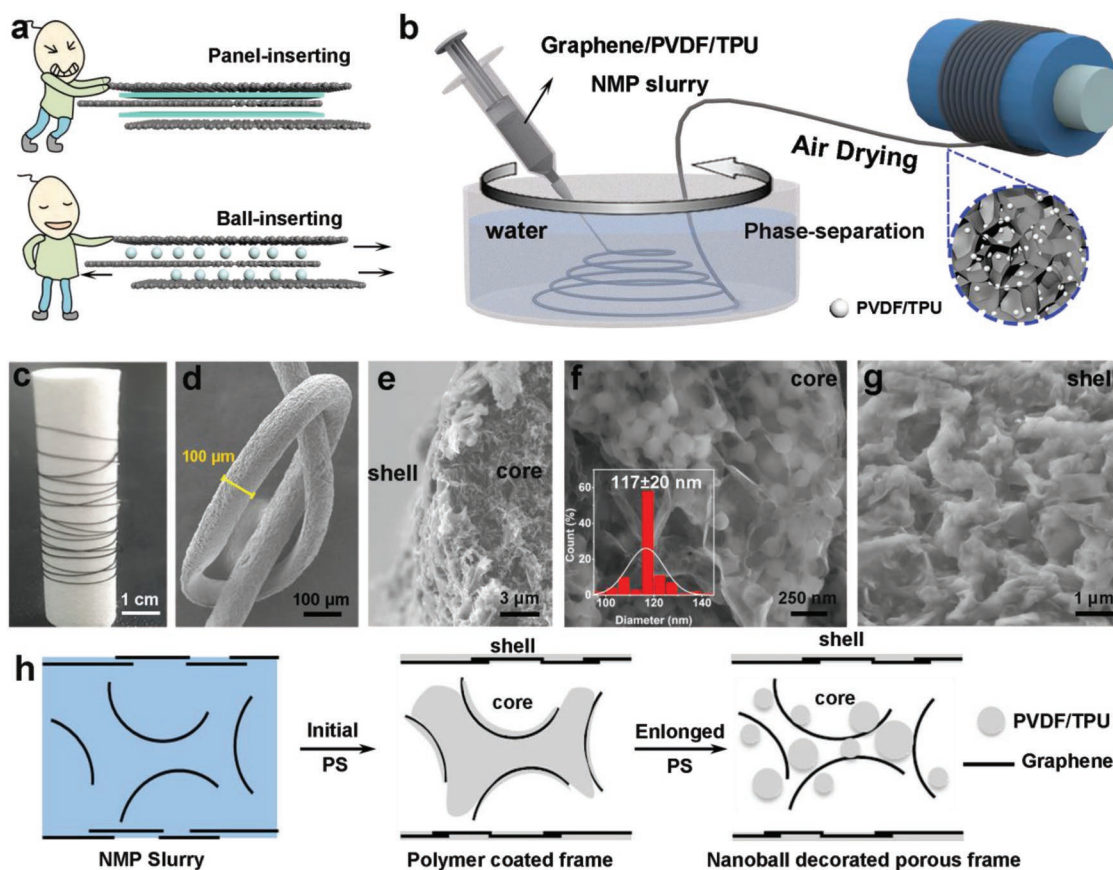


**Figure 1.** Fabrication of PGFs. a) Schematic illustrating the comparison between a panel inserting and nanoballs inserting for reducing interconnection of layer. b) Schematic of the successive fabrication process for PGFs. The blue dashed circle marks the schematic structure of PGFs. c) Digital photograph of PGFs collected on the roll. d) The low-resolution SEM image of knotted PGFs. e) Cross-sectional SEM images of PGFs showing the core-shell structure. f) SEM image of core structure with transparent graphene sheets and polymer nanoballs. The inset shows the average diameter:  $117 \pm 20$  nm. g) SEM image of surface with the polymer shell. h) Schematic illustration of the formation process of the porous nanoball-decorated structure in the PGFs.

were reported to have gauge factor ( $GF = 29$ ), but this kind of composite fibers normally shows  $GF$  less than 30.<sup>[12,24]</sup> Theoretically, the  $GF$  is determined by the ratio between the relative resistance change ( $\Delta R/R_0$ ) and the applied strain ( $\epsilon$ ).<sup>[6]</sup> High sensitivity requires large resistance change under the same strain. The resistance change relies on the connection changes of conductive pathways formed by the conductive units or on the deformation of conductors.<sup>[12]</sup> However, for graphene polymer fibers with normal structure, the connection change is suppressed by the structure integrity of composite, leading to a much lower sensitivity especially in low strain range.

Inspired by the rolling friction in daily life, we try to decrease the interconnection of graphene sheets and polymer by reducing the contact area as illustrated in **Figure 1a**. Herein, we designed porous graphene fibers (PGFs) inserted with polymer nanoballs between graphene sheets. Polyvinylidene fluoride (PVDF) is chosen because it can present a globular morphology through phase separation (PS) method.<sup>[25]</sup> The PGFs exhibit high gauge factors (51 in 0–5%, 87 in 5–8%) and a low detection limit (1/10 000 of strain). Besides, the inclusion of polyurethane (PU) in the nanoball-decorated structure confers the PGFs with long term durability (more than 6000 times cycles).

To demonstrate the possible practical application, the PGFs were integrated into daily garments to monitor the pulse, motions, and eyeball movement. They were also used to be woven into specially designed electronic fabrics for real-time and two-point position sensing.

## 2. Results and Discussion

### 2.1. Characterization

Figure 1b illustrates the PGFs fabrication process. We chose high-quality graphene dispersed in N-methylpyrrolidone (NMP) ( $20 \text{ mg mL}^{-1}$ ) for its structural integrity and high conductivity to fabricate the PGFs.<sup>[26,27]</sup> The graphene/NMP slurry was then mixed with PVDF and PU for further wet-spinning. As shown in Figure 1b, a revolving water sink (110 rpm) was used as the coagulation basin and the graphene/PVDF/PU slurry was then injected into the water. A solid phase formed as soon as the slurry was injected and continuous graphene composite fibers could be drawn out due to the shear force created by the water flow.<sup>[28]</sup> After sufficient air drying, the PGFs were

collected on a roll (Figure 1c). Field emission scanning electron microscope (FE-SEM) was used to observe the microstructure of PGFs. The knot in Figure 1d illustrates the high flexibility of PGFs. The obtained fibers were about 100  $\mu\text{m}$  in diameter. Transmission electron microscopy (TEM) and in-situ SEM-Raman mapping show that the high-quality graphene sheets disperse in the PGFs (Figures S1 and S2, Supporting Information). The high-resolution cross-section image clearly shows the core-shell structure of the PGFs (Figure 1e). The core decorated with polymer nanoballs has pores (Figure 1f) whereas the shell without nanoballs is denser (Figure 1g). Figure 1f shows the transparent graphene sheets with many polymer nanoballs (average diameter:  $117 \pm 20$  nm). Unlike the nanoball-filled core, the shell shows the thick polymer covering the graphene sheets (PVDF/PU, Figure S3, Supporting Information), as shown in Figure 1g.

In fact, above nanoball-decorated structure can only be obtained by prolonging the PS time during wet-spinning. During the beginning 5 s of the PS process, a porous structure without nanoballs is formed. And many polymer humps emerged on the surface of graphene sheets after 60 s of PS (Figure S4, Supporting Information). Then, the humps became larger and many nanoballs could be observed after 120 s of PS. After 180 s, a large number of nanoballs was observed, which indicated that the time required to form porous nanoballs decorated graphene fibers was about 3 min (Figure S4, Supporting Information). Actually, the morphology of the phase-separated pure PVDF was affected by the mass-transfer rate of the nonsolvent. At a high rate, the rapid increase of the nonsolvent concentration leads to a metastable region between the binodal and spinodal curves in the ternary phase diagram of the PVDF-solvent-nonsolvent system (Figure S5, Supporting Information). In this region, a bicontinuous morphology is formed

during PS. But at lower rate, the concentration of the nonsolvent changed slowly, the composition crossed the spinodal curve and entered an unstable region over spinodal, where spinodal decomposition process dominated and PVDF formed the nanoball structure.<sup>[25]</sup> In our investigation, pure PVDF fibers and PGFs have a similar core-shell structure (Figure S5, Supporting Information). Therefore, the mass-transfer theory of PVDF can also be used to explain the structure formation of PGFs. Shell with a bicontinuous morphology was formed due to the rapid introduction of water on the surface of the composite slurry containing PVDF. The dense shell formed then slowed down the subsequent mass transfer of water into the inner area, finally leading to the domination of PS by spinodal decomposition with nanoballs loosely dispersed on the graphene sheets. Due to the suppressed mass transfer of water and the slow PS process, the formation of nanoballs needs more time to complete. If stopped early, the inner polymer solidifies and the process can only complete through the drying and evaporation of the residual NMP, as shown in Figure 1h. This is detrimental to the formation of nanoballs, as observed in the phase-separated samples at 5, 60, and 120 s. Consequently, at least 180 s of PS is necessary to form the loose globular spherulites (Figure 1h). Nevertheless, numerous pores were observed regardless of the PS time. The formation of pores occurs simultaneously with polymer densification. Polymer densification cannot completely fill out the frame formed by graphene sheets whether a bicontinuous or nanoballs are formed or not, leading to the porous structure.

To investigate the superiority of the nanoball-decorated structures as strain sensors, the structural characterization was performed. As shown in Figure 2a, different cross-sections of the graphene/PVDF/PU samples were observed through SEM with the same component: i) porous nanoball-decorated structure

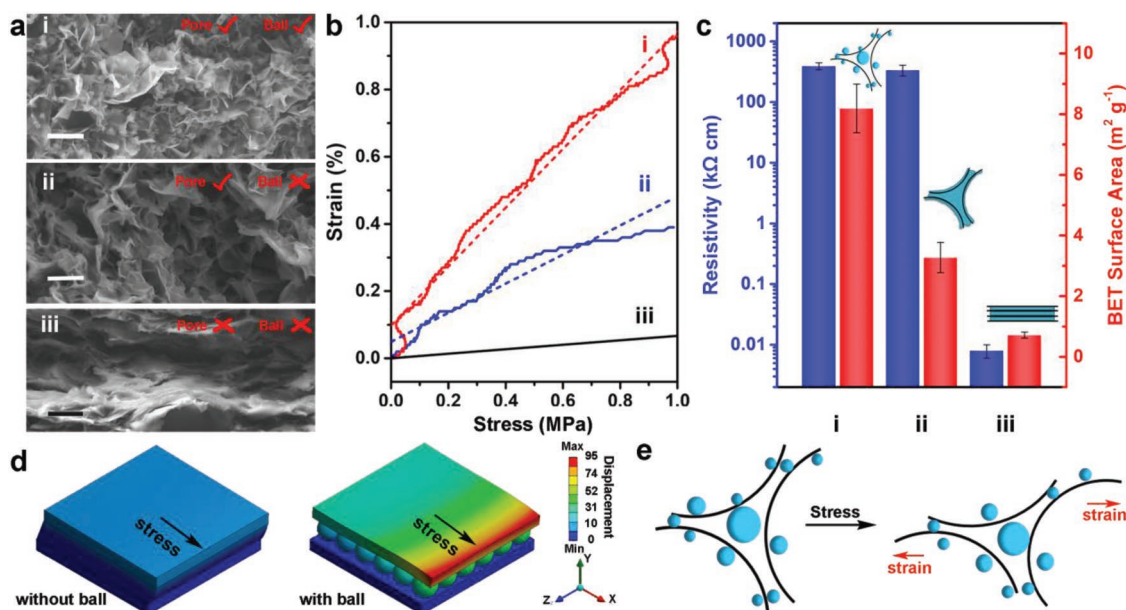


**Figure 2.** Structural Characterization of PGFs. a) SEM images of the different structures (i) with pores and nanoballs, (ii) with pores but without nanoballs, and (iii) without pores or nanoballs. Scale-bar: 1  $\mu\text{m}$ . b) Compliance curve of the structures (i–iii) in (a). c) Resistivity and BET surface area histograms for the different structures in (a). d) Displacement comparison between nanoball-free (left) and nanoball (right) structures as analyzed by finite element simulation (FES). e) Illustration of the sensitivity of the porous nanoball-decorated structure.

of PGFs, ii) porous structure without nanoballs, and iii) dense film without nanoballs nor pores. Figure 2a-(iii) shows the regular stack of the graphene sheets and polymers. Figure 2a-(ii) shows the overall porous structure without nanoballs. In contrast, the transparent graphene sheets are clearly recognizable and numerous polymer nanoballs decorate the graphene frame, as shown in Figure 2a-(i). The dense film in Figure 2a-(iii) was fabricated by the natural evaporation of the solution (Supporting Information). The structural integrity of the different structures was established via a stress test. Figure 2b shows the strain–stress curve of the structures-(i), (ii), and (iii) (Figure S6, Supporting Information). The slope of the curve denotes the mechanical compliance ( $C$ ) of composites, which is defined as

$$C_x = \partial \varepsilon / \partial \sigma \quad (1)$$

where  $\varepsilon$  and  $\sigma$  represent the strain and stress, respectively. As the dashed lines shown in Figure 2b,  $C_i$  ( $0.875 \text{ MPa}^{-1}$ ) is much larger than  $C_{ii}$  ( $0.433 \text{ MPa}^{-1}$ ) and  $C_{iii}$  ( $0.066 \text{ MPa}^{-1}$ ). The higher mechanical compliance of the porous nanoball-decorated structure contributes to larger structure deformation than other structures for the same strain, which allows a higher sensitivity of the PGFs.<sup>[29]</sup> In contrast, the stiff graphene/PVDF/PU film without pores nor nanoballs is harder to deform. To further understand the difference between the nanoball-decorated structure-(i) and the nanoball-free structure-(ii), the resistivity and the BET surface area were determined, as shown in Figure 2c (Figure S7, Supporting Information).

The conducting networks of the composite are formed by the contact between high-quality graphene sheets.<sup>[30]</sup> In other words, the variation in resistivity for the composite originates from the changes of graphene frame. The pore-less structure of the graphene/PVDF/PU film has low resistivity ( $0.008 \pm 0.002 \text{ k}\Omega \text{ cm}$ ) for the tight stack of the graphene sheets. Structure-(i) has higher resistivity of  $393 \pm 69 \text{ k}\Omega \text{ cm}$  and structure-(ii) shows a resistivity of  $337 \pm 50 \text{ k}\Omega \text{ cm}$ , indicating that the porous graphene frame has a smaller contact area. However, the difference in resistivity between structure-(i) and (ii) is not significant, which suggests that their conducting networks (graphene frames) are almost the same. This is also evidenced by the numerically close porosity of structure-(i) and (ii) (Figure S8, Supporting Information). Besides, the increase of porosity from structure-(iii) to (i)/(ii) explains the larger stretchability than layer-by-layer stacking structure because the porous structure potentially provides larger space than layer-by-layer stacking via bending of network skeletons or rotating of pore walls toward the stretching direction.<sup>[31]</sup> The BET surface area results of structure-(i) to (iii) reflect the structural variation more precisely. Structure-(ii) has a larger specific area than structure-(iii) because of the graphene frame. However, the specific area of structure-(i) is larger than (ii) even if they have the same graphene frame. It is obvious that, due to the formation of nanoball structure, the finer spaces between the nanoballs increase the specific area, which explains the higher compliance of the porous/nanoball structure. To further underline the superiority of the nanoball structure over the nanoball-free structure, finite element simulations (FES) were conducted to forecast the sensitivity (Tables S1 and S2, Supporting Information), as shown in Figure 2d. The dense polymer layer (PVDF)

inserted in the two graphene sheets generates a much smaller displacement than the nanoball structure when the same stress is applied, which agrees well with the compliance results. The designed graphene frame in the PGFs undergoes larger structural variations and more conducting-network changes, which explains higher sensitivity (Figure 2e). The performance data of the PGFs sensors is required to confirm their higher sensitivity.

After their assembly on the silver electrodes (Figure S9, Supporting Information), strain-sensor devices were fabricated from fibers with three different structures. The typical resistivity-strain curves for the PGFs strain sensors (strain speed,  $0.01 \text{ mm s}^{-1}$ ) are shown in Figure 3a (Supporting Information). The dark, blue, red, and green curves represent the relative resistance change of the pore-less/nanoball-free, the porous/nanoball-free, the porous/nanoball-decorated, and the simple PU/graphene sensors, respectively. The slope of the resistance change versus the strain determines the GF, which is defined as

$$\text{GF} = (\Delta R / R_0) / \varepsilon \quad (2)$$

where  $\Delta R$ ,  $R_0$ , and  $\varepsilon$  represent the change of resistance, the resistance at 0% strain, and the applied strain, respectively.<sup>[32]</sup> It is noticeable that nanoball-decorated PGFs (red curve) show high GF of 51 ( $R^2 = 0.98$ ) under 0–5% strain and 87 at 5–8% strain ( $R^2 = 0.99$ ), which is almost 10 times larger than nanoball-free PGFs (GF = 5, blue curve in Figure 3a). Seldom did reported fiber-based strain sensors reach such high GF and show good linear fit (0–10% strain) as shown in Table 1. The reported graphene decorated fibers/textiles for which graphene was coated directly onto the fabrics had a relatively low GF of 26.<sup>[7]</sup> Graphene fibers obtained by chemical vapor deposition (CVD) process had a much lower GF (5) due to polymer shell encapsulation.<sup>[33]</sup> Ag- or Au-decorated fibers had a good GF of about 35 because the rigid metal coating generates much easier conducting net variation.<sup>[34,35]</sup> As we designed, the PGFs with polymer nanoballs reduced the strong interaction to yield a GF almost 1.5 times higher than Ag- or Au-decorated fibers in the tested strain range of 0–30%. The graphene/PVDF/PU film (black curve in Figure 3a) also had a very low GF of 6.5 (Figure S10, Supporting Information) and an extremely low strain range of 0–0.8%. The normal PU/graphene composite (green curve) had a GF of 2 in the strain range of 0–10% even with a higher working range (0–50%). Therefore, the higher GF of the porous/nanoball-decorated structure makes it more sensitive than previously reported structures. Recently, Liu et al. reported a surface-strain-redistribution strategy that could enhance the sensitivity of fiber-shaped stretchable strain sensors by introducing beads.<sup>[36]</sup> We adopted this strategy to fabricate PGFs with beads (beads-PGFs) by controlling the rate of extrusion in wet spinning process. Testing results (Figure S11, Supporting Information) shows further increase of the GF to 54 (0–5% strain) and 108 (5–7.8% strain), which shows the potential of the proposed interconnection structure and PGFs combining with other strategies to further improve the strain performance.

Figure 3b shows the  $\Delta R/R_0$ – $\varepsilon$  curve for the stretch-release of PGFs under different strains. Under applied strains 1% and 2%, the net  $\Delta R/R_0$  variation is small, which means that the elastic

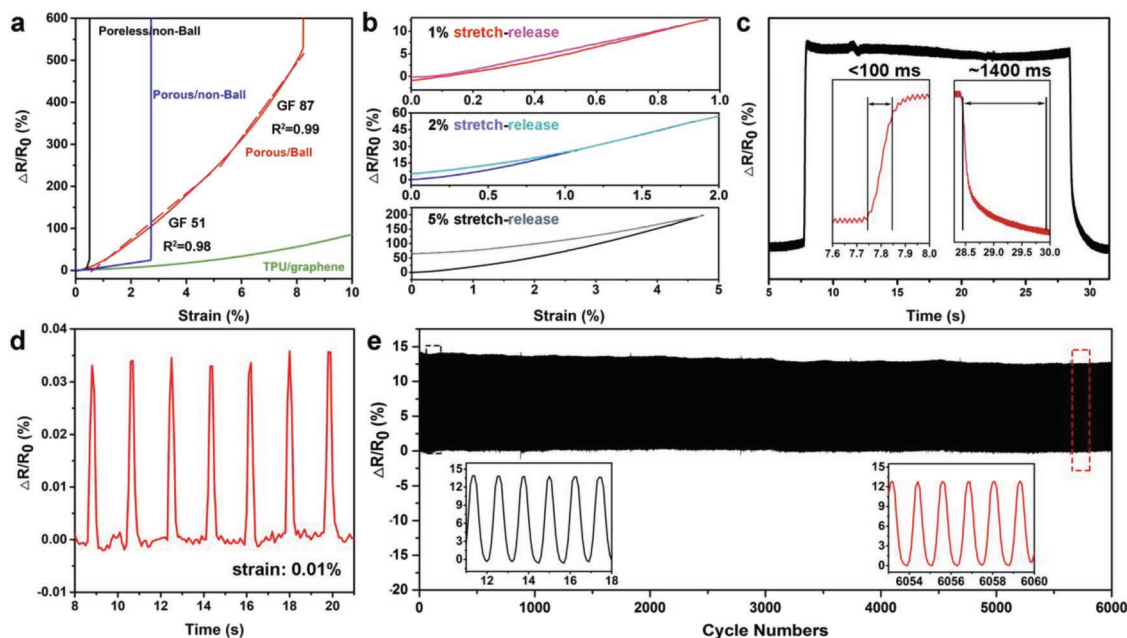


**Figure 3.** Sensing properties of PGFs. a) Gauge factors for pore-less/nanoball-free (black), porous/nanoball-free (blue), porous/nanoball (red), and TPU/graphene control (green). b) Stretch and release curves under a 1%, 2%, and 5% strain (top to bottom). c) Response time of the PGFs strain sensors. d) The testing limit of the PGFs reaches 0.01% (SNR: 26 dB). e) Durability of the PGFs strain sensors after 6000 cycles at a 1% strain stretch and release.

PU/PVDF shell allows PGFs structure to recover in the 0–2% strain range. Repeated stretch-release cycles for an applied strain within 0.1–2% illustrating the short cycling stability of PGFs under 2% strain (Figure S12, Supporting Information). However, strains higher than 5% lead to rather larger changes from the original resistance, which suggests an irreversible structure deformation. Besides, the bending of the PGFs generates a negative change in the resistance to possibly detect intricate signals (Figure S13, Supporting Information). To determine the response time, the sensor was loaded with a quasi-transient step of 0.5% strain (Supporting Information). The response time was less than 100 ms according to the real-time high-resolution  $\Delta R/R_0$ - $t$  response curves (Figure 3c). However, the recovery time was about 1400 ms. The longer recovery time is due to the weak inner strength of the PGFs that cannot

support the rapid recovery of the structure. This fast response undoubtedly facilitates real-time monitoring of fast and intricate signals in the human body. The detection limit for the PGFs devices should be more important when a higher sensitivity was obtained. As shown in Figure 3d,  $\Delta R/R_0$  for the PGFs can reach 0.034% with signal to noise ratio (SNR) of 26 dB for an applied strain of 0.01%. As shown in Table 1, the rGO-covered double yarn showed 0.2% detection limit.<sup>[6]</sup> The detection limit of the Ag nanowires incorporated with polyurethane was 0.065% strain and that of the carbon nanotubes (CNT) decorated fiber was only 1% strain.<sup>[15,37]</sup> And the carbonized cotton fabric shows 0.02% detection limit.<sup>[39]</sup> Using the nanoball-decorated porous structure, 1/10 000 strain can be detected, which is more sensitive than other reported structures. However, the long circling stability of the PGFs sensors should be considered

**Table 1.** Properties of the different methods for flexible fiber-based strain sensors.

Materials	GF	Detection limit	Cycling stability	Reference
rGO coated double covered yarn	10(0–50%)	0.2%	N/A	[6]
Graphene coated polyester	26 (0–14%)	N/A	>500	[7]
Graphene fiber core/polymer shell	5.02 (1–6.3%)	N/A	>200	[33]
Ag nanowires/PU fabric	<50(0–30%)	0.065%	>4500	[15]
Ag-shell multifilament fiber	35(0–120%)	N/A	>10 000	[34]
Au-CNT-PDMS fiber	36(0–120%)	N/A	>5000	[35]
CNT sheet/rubber/fiber	0.5 (0–200%)	1%	>5000	[37]
Conductive yarn textile	7.5(0–50%)	N/A	>2500	[38]
Carbonized cotton fabric	25 (0–80%)	0.02%	>2000	[39]
Graphene/PVDF/PU	51 (0–5%) 87 (5–8%)	0.01%	>6000	This work

for daily usage. Over 6000 stretch-release cycles were performed at 1% strain, as shown in Figure 3e. For all cycles, the whole curve was stable and  $\Delta R/R_0$  almost remained constant. The inserting images of Figure 3e indicate that the net  $\Delta R/R_0$  for 5000 cycles is 13, which is almost the same with the first 12 cycles (14). Even after many cycles of structural deformation with repeated stretching, the structure inserted with nanoballs still has the same sensitivity, proving that it is well-suited for real applications. Meanwhile, the high gauge factor, the long durability, the low detection limitation, and the fast response time show great promise for the PGFs to be used as wearable strain sensors.

## 2.2. Applications

To test their application as wearable sensors, we integrated the PGFs onto commercial bandage without polymer encapsulating and pasted it on the wrist to collect pulse signals (Figure 4a). The pulse is a very important but relatively small physiological signal for systolic and diastolic blood pressure as well as to determine the heart rate.<sup>[40]</sup> As shown in Figure 4b, the pulse signals are very clear and show beats rate of 68 min<sup>-1</sup>. The insert (black curve) shows a close-up of a single pulse peak and clearly produces the typical characteristics of the pulse waveform, namely the percussion wave (P wave), the tidal wave (T wave), and the diastolic wave (D wave).<sup>[41]</sup> If the vein is pressed, the intensity of the signal (red curve) is lower than the normal signal and the frequency of the pulse decreases to about 60 min<sup>-1</sup>, illustrating the high sensitivity of the PGFs to distinguish a small change. The arterial neck pulse can also be determined using the PGFs based sensors (Figure S14, Supporting Information). The movement of the fingers can generate a

remarkable resistance change, as illustrated in Figure 4c. Finger bending will lead to a larger signal change, indicating accurate motion detection capability. Furthermore, the PGFs can be woven into fabric for wearable sensor application. Here, we wove the PGFs into a gauze piece shaped as a “serpentine” (S) and integrated electrodes into the gauze. The integration with the fabric increases the stretchability of the PGFs, as shown in the insert of Figure 4d, but decreases the GF to about 10 (Figure S15, Supporting Information). The test range of the woven PGFs was over 100%, which was 10 times larger than the unwoven fiber. The large deformation of the gauze fabric dissipates evenly on the woven PGFs. The dissipated deformation is reflected in the resistance change. Figure 4d shows that the resistance change creates a different response for applied strains of 20%, 50%, and 100%. It also proves that the woven PGFs can adapt to different conditions.

For a more practical application, we wove PGFs into a gauze (Figure 4e) to monitor eyeball movement. Normal eye-monitors using membranes make people uncomfortable because they

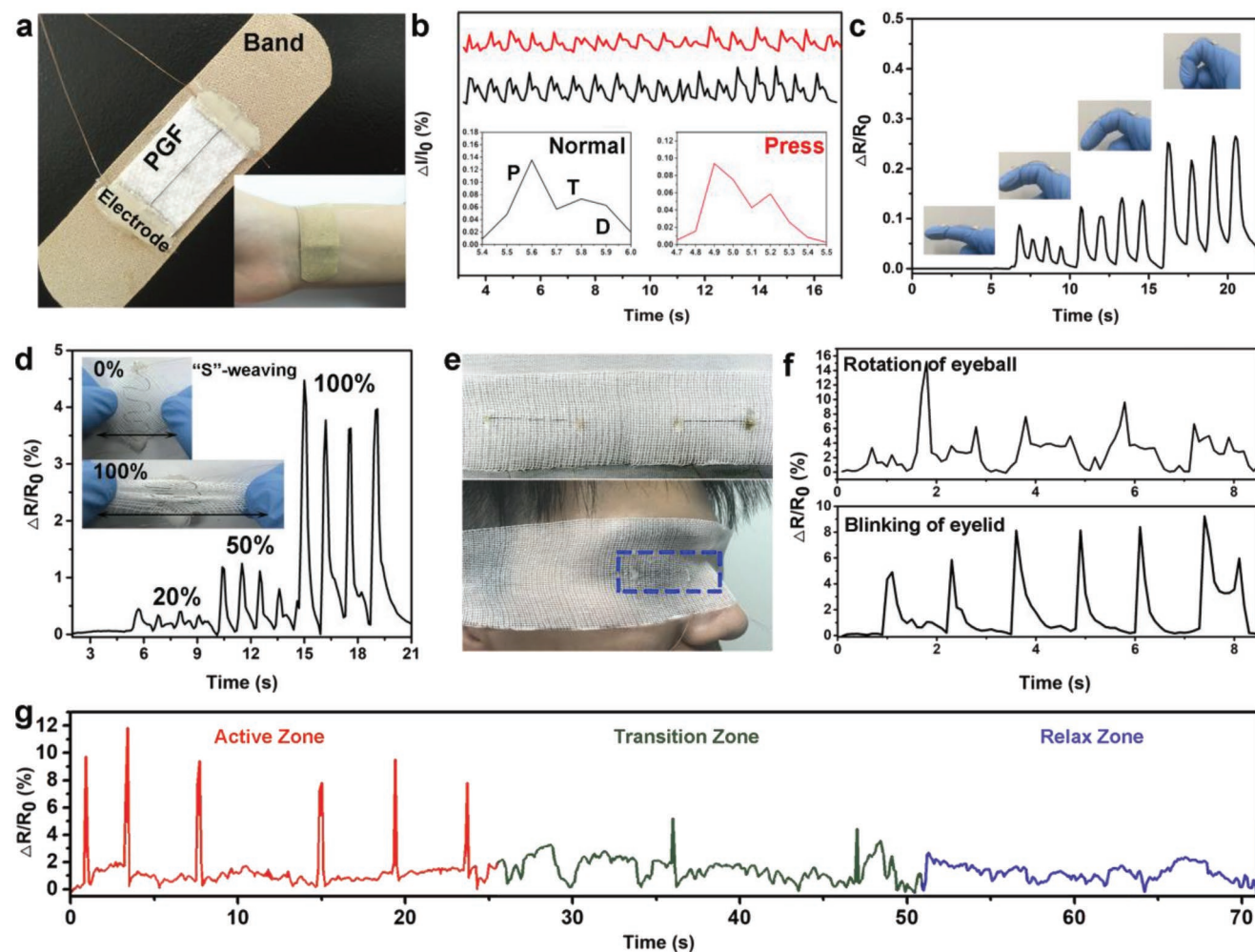


**Figure 4.** Applications of PGFs-based strain sensors. a) Digital photographs of the PGFs fibers integrated into a bandage and sticking on the wrist. b) Wrist pulse resistance in the normal and pressed states. The inset shows the detailed information of the pulse using the PGFs sensors. c) The signal when the PGFs are used to monitor finger bending. d) Resistance changes of weaved PGFs sensors with increasing stretching. The inset is the digital photographs of weaving the PGFs with gauze, showing the higher stretching range. e) Digital photographs of the homemade eyeball monitoring device. f) Signals from eyeball rotation and blinking. g) Real-time monitoring of the eyes during sleep.

stick to the face. PGFs decorated gauze is more comfortable than a commercial eye patch and its strain sensors may be applied for the monitoring on the patients with eye diseases. A typical eyeball movement contains the rotation of eyeball and the blinking of the eyelid. These two movements of the eyeball can create different  $\Delta R/R_0$  changes, as shown in Figure 4f. The  $\Delta R/R_0$  of the eyelid blinking is narrow but that of the eyeball rotation is wider. We used this eye-monitor to follow the eyeball movement during a nap. Figure 4g shows the three typical regions: activity, transition, and relaxing. At first, the eyes show intensive eyeball movement with blinking or rotation. After a few seconds, the frequency of the blinking decreases and the rotation of the eyeball is the main movement. A few minutes later, the eyes relax and the signals become weak. With such an ultrasensitive structure, minute signals of eyeball motion can be detected. Also, the weaving capability promises better wearable sensing.

Furthermore, to test the feasibility of tactile sensing for smart textiles, it is desirable to weave the PGFs sensors into textile sensing array to map the resolved deformation information. Figure 5a schematically describes the  $3 \times 3 \times 3$  matrix model based on  $x$ - $y$ - $z$  three axis sensing arrays (ternary system) woven fabric. Every set of PGFs sensors on each axis records the real-time resistance change. The sensing array is completely flexible and can be easily integrated with cloth, as shown in Figure 5b. Every crossed point corresponds to a unique location (P1–P6). The relative resistance changes at these locations ( $\Delta R_{p_i}$ ) were calculated from Equation (3)

$$\Delta R_{p_i} = (\Delta R_{x_i} + \Delta R_{y_j} + \Delta R_{z_k})/3 \quad (3)$$

where  $\Delta R_{x_i}$ ,  $\Delta R_{y_j}$ , and  $\Delta R_{z_k}$  represent the relative resistance changes of the PGFs placed at each location (Figure S16, Supporting Information). When the finger was placed on one

of the cross points of the  $x$ - $y$ - $z$  axes (P4 in Figure 5c), the output  $\Delta R_{p_4}$  could represent the touching location. A normal binary weaving method (two-axis) cannot achieve multipoint sensing (Figure S17, Supporting Information). However, our ternary weaving method can distinguish between two locations at the same time. Two locations (P2 and P5) could be distinguished by the ternary weaving system, as illustrated in Figure 5c. This result proves that fiber-based strain sensors have the potential to achieve multipoint touching for special usage. Such weavable sensitive PGFs are very promising for intelligent wearable personal care sensors or for human-computer interaction.

### 3. Conclusions

In summary, we propose a versatile and facile approach to prepare highly sensitive nanoball-decorated PGFs. By combining polymer nanoballs and graphene sheets, the designed fibers have high gauge factors (51 within 0–5% and 87 within 5–8%), a stable cycling performance (for 6000 cycles), a fast response time (<100 ms), and a low detection limit (0.01% strain). The PGFs sensors can detect various information, including the real-time monitoring of a pulse wave, joint motion, and eyeball movement. The PGFs were also integrated into commercially available fabrics for spatially mapping tactile stimuli. Given the low-cost rapid fabrication method, the high performance, and the flexibility obtained, this fabricated PGFs sensor has a great potential in future wearable electronics. Besides, the interconnection weakening strategy provides a new solution to increase sensitivity of strain sensors and the materials used may be expanded to other conductive particles and polymers that can form the nanoball-decorating structure through phase separation or other methods.

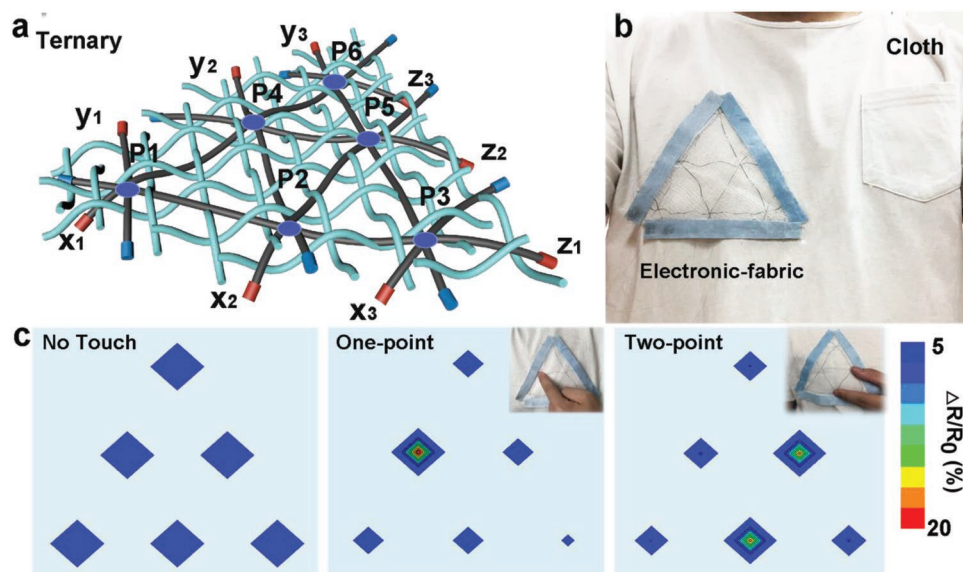


**Figure 5.** Electronic fabrics when weaving the PGFs into textiles. a) 3D models of the PGFs woven in the ternary matrix,  $x_i$ - $y_j$ - $z_k$  letters represent the woven PGFs and the  $P_j$  letters represent the locations. b) Digital photographs of the electronic fabric integrated with commercial cloth. c) The resistance reflection of no touch, one-point touch, and two-point touch.

## 4. Experimental Section

**Materials:** Sodium persulfate ( $\text{Na}_2\text{S}_2\text{O}_8$ ,  $\geq 99$  wt%, Sinopharm), sulfuric acid ( $\text{H}_2\text{SO}_4$ , 95–98 wt%, Sinopharm), PVDF powder (molecular weight: 107 000, Sigma), polyurethane (PU, 1180A, BASF), and N-Methyl pyrrolidone (NMP, AR, Sigma) were purchased and used as received without further purification. Graphite powder (325 mesh) were purchased from Qingdao Xinghe graphite Co., Ltd. (Qingdao, China).

**Fabrication of Graphene/NMP Slurry:** The graphene used in this work was prepared through an enhanced bubble-exfoliation method.<sup>[26]</sup> More specifically, a reaction mixture composed of 1 g graphite, 10 g  $\text{Na}_2\text{S}_2\text{O}_8$ , and 90 mL sulfuric acid was kept at room temperature for 10 min under constant stirring. Then, the mixture was transferred to a preheated kettle and maintained at 80 °C for 30 min under constant stirring (350 rpm). The product was isolated by filtration and the filtrate was collected for the next graphite exfoliation cycle. After thorough rinsing with water and ethanol, the product was dried at 50 °C in ambient air for 5 h to obtain a fluffy powder. Then, it was dispersed in NMP to obtain the graphene/NMP slurry.

**Fabrication of the PGFs Fiber:** PVDF and PU were dissolved into 2 mL of warm NMP (60 °C), with a weight ratio of 1:3. 5 mL of Graphene/NMP slurry were mixed with the PVDF/PU solution and dispersed by ultrasonication for 2 h to obtain a homogeneous graphene/PVDF/PU slurry. The slurry was then injected into water for PS. After allowing sufficient time for the PS to occur, the PGFs were drawn out and collected on a roll.

**Integration of the PGFs Strain Sensor:** The PGFs were cut to 4 cm in length and placed onto a polydimethylsiloxane slab of 60 mm × 10 mm × 3 mm (10:1 mixture of prepolymer and curing agent, Sylgrad-184, Dow Corning). Silver paste was used on the two ends of the PGFs and copper wires (100  $\mu\text{m}$  in diameter) were used to connect with the Ag slurry. After heat drying (80 °C, 30 min), both ends of the electrode were sealed with silicone rubber.

**Integration of the PGFs Fabric into a Wearable Sensor:** The gauze was cut into desired shape. For the stretchable gauze, the cut followed the diagonal of the textile direction. The long PGFs (30 cm) was woven into the gauze manually. The electrodes were sealed at both ends of the woven PGFs as mentioned above.

**Characterization:** Raman imaging and scanning electron microscopy (RISE, WITec, Germany) is a new and unique analysis tool which combined scanning electron microscopy (SEM, TESCAN MIRA3) and Raman Spectroscopy with a laser excitation at 532 nm. The conductivity of the PGFs and the film with various structures was obtained with an electrochemical workstation CHI660E (scanning speed: 0.1 V s<sup>-1</sup>, voltage range: -4 to 4 V). BET specific area was obtained using a Micromeritics TriStar 3020 under N<sub>2</sub> atmosphere. The stress-strain properties were measured with a high-precision electronic universal testing machine (CMT6103, MTS Systems, China Co., Ltd.). For strain sensing, the strain load was implemented with a high-precision motorized linear stage (displacement resolution of 2.5  $\mu\text{m}$ ). A constant voltage of 1 V was applied to the fiber sensor to acquire a real-time current signal using an electrochemical workstation (PARSTAT 2273, Princeton Applied Research). Informed signed consent for publication of the data has been obtained from the volunteers who participated in this work.

## Supporting Information

Supporting Information is available from the Wiley Online Library or from the author.

## Acknowledgements

The authors thank Dr. Zhu Xu of Changzhou University for the finite element simulations. The authors thank Dr. Wei Li of TESCAN China for the RISE instrument and for his great suggestions and help with the SEM and Raman measurements. This work was supported by the

National Natural Science Foundation of China (Grants 51802337, 11774368, and 11804353), China Postdoctoral Science Foundation (Grant BX201700271), and STCSM (18511110600).

## Conflict of Interest

The authors declare no conflict of interest.

## Keywords

electronic fabrics, nanoballs, porous graphene fibers, strain sensors

Received: May 10, 2019

Revised: July 6, 2019

Published online:

- [1] M. Liu, X. Pu, C. Y. Jiang, T. Liu, X. Huang, L. B. Chen, C. H. Du, J. M. Sun, W. G. Hu, Z. L. Wang, *Adv. Mater.* **2017**, *29*, 1703700.
- [2] C. Y. Wang, K. L. Xia, H. M. Wang, X. P. Liang, Z. Yin, Y. Y. Zhang, *Adv. Mater.* **2019**, *31*, 1801072.
- [3] M. Amjadi, K. U. Kyung, I. Park, M. Sitti, *Adv. Funct. Mater.* **2016**, *26*, 1678.
- [4] W. Zeng, L. Shu, Q. Li, S. Chen, F. Wang, X. M. Tao, *Adv. Mater.* **2014**, *26*, 5310.
- [5] L. B. Hu, Y. Cui, *Energy Environ. Sci.* **2012**, *5*, 6423.
- [6] Y. Cheng, R. R. Wang, J. Sun, L. Gao, *Adv. Mater.* **2015**, *27*, 7365.
- [7] Z. Yang, Y. Pang, X. L. Han, Y. F. Yang, J. Ling, M. Q. Jian, Y. Zhang, Y. Yang, T. L. Ren, *ACS Nano* **2018**, *12*, 9134.
- [8] Y. Wei, S. Chen, X. Yuan, P. Wang, L. Liu, *Adv. Funct. Mater.* **2016**, *26*, 5078.
- [9] Y. L. Wang, J. Hao, Z. Q. Huang, G. Q. Zheng, K. Dai, C. T. Liu, C. Y. Shen, *Carbon* **2018**, *126*, 360.
- [10] Z. Q. Song, W. Y. Li, Y. Bao, F. J. Han, L. F. Gao, J. Xu, Y. M. Ma, D. X. Han, L. Niu, *ACS Appl. Mater. Interfaces* **2018**, *10*, 42826.
- [11] T. Yamada, Y. Hayamizu, Y. Yamamoto, Y. Yomogida, A. Izadi-Najafabadi, D. N. Futaba, K. Hata, *Nat. Nanotechnol.* **2011**, *6*, 296.
- [12] Y. R. Jeong, H. Park, S. W. Jin, S. Y. Hong, S. Lee, J. S. Ha, *Adv. Funct. Mater.* **2015**, *25*, 4228.
- [13] X. M. Li, T. Yang, Y. Yang, J. Zhu, L. Li, F. E. Alam, X. Li, K. L. Wang, H. Y. Cheng, C. T. Lin, Y. Fang, H. W. Zhu, *Adv. Funct. Mater.* **2016**, *26*, 1322.
- [14] J. Ryu, J. Kim, J. Oh, S. Lim, J. Y. Sim, J. S. Jeon, K. No, S. Park, S. Hong, *Nano Energy* **2019**, *55*, 348.
- [15] W. S. Lee, S. W. Lee, H. Joh, M. Seong, H. Kim, M. S. Kang, K. H. Cho, Y. M. Sung, S. J. Oh, *Small* **2017**, *13*, 1702534.
- [16] B. Park, J. Kim, D. Kang, C. Jeong, K. S. Kim, J. U. Kim, P. J. Yoo, T. I. Kim, *Adv. Mater.* **2016**, *28*, 8130.
- [17] Y. N. Yang, L. J. Shi, Z. R. Cao, R. R. Wang, J. Sun, *Adv. Funct. Mater.* **2019**, *29*, 1807882.
- [18] W. B. Zhong, C. Liu, C. X. Xiang, Y. X. Jin, M. F. Li, K. Liu, Q. Z. Liu, Y. D. Wang, G. Sun, D. Wang, *ACS Appl. Mater. Interfaces* **2017**, *9*, 42058.
- [19] L. T. Yu, J. C. Yeo, R. H. Soon, T. Yeo, H. H. Lee, C. T. Lim, *ACS Appl. Mater. Interfaces* **2018**, *10*, 12773.
- [20] D. Ponnammam, Q. Guo, I. Krupa, M. A. S. A. Al-Maadeed, K. T. Varughese, S. Thomas, K. K. Sadasivuni, *Phys. Chem. Chem. Phys.* **2015**, *17*, 3954.
- [21] H. Cheng, J. Liu, Y. Zhao, C. G. Hu, Z. P. Zhang, N. Chen, L. Jiang, L. T. Qu, *Angew. Chem., Int. Ed.* **2013**, *52*, 10482.



- [22] G. Y. Li, G. Hong, D. P. Dong, W. H. Song, X. T. Zhang, *Adv. Mater.* **2018**, *30*, 1801754.
- [23] Z. Xu, Y. J. Liu, X. L. Zhao, L. Peng, H. Y. Sun, Y. Xu, X. B. Ren, C. H. Jin, Pe. Xu, M. Wang, C. Gao, *Adv. Mater.* **2016**, *28*, 6449.
- [24] S. Cravanzola, G. Haznedar, D. Scarano, A. Zecchina, F. Cesano, *Carbon* **2013**, *62*, 270.
- [25] T. H. Young, L. P. Cheng, D. J. Lin, L. Fane, W. Y. Chuang, *Polymer* **1999**, *40*, 5315.
- [26] P. He, H. Y. Gu, G. Wang, S. W. Yang, G. Q. Ding, Z. Liu, X. M. Xie, *Chem. Mater.* **2017**, *29*, 8578.
- [27] H. X. Tang, P. He, T. Huang, Z. Y. Cao, P. L. Zhang, G. Wang, X. Y. Wang, G. Q. Ding, X. M. Xie, *Carbon* **2019**, *143*, 559.
- [28] T. Huang, S. W. Yang, P. He, J. Sun, S. Zhang, D. Li, Y. Meng, J. S. Zhou, H. X. Tang, J. R. Liang, G. Q. Ding, X. M. Xie, *ACS Appl. Mater. Interfaces* **2018**, *10*, 30732.
- [29] S. Xu, Y. H. Zhang, L. Jia, K. E. Mathewson, K. I. Jang, J. Kim, H. R. Fu, X. Huang, P. Chava, R. H. Wang, S. Bhole, L. Z. Wang, Y. J. Na, Y. Guan, M. Flavin, Z. S. Han, Y. G. Huang, J. A. Rogers, *Science* **2014**, *344*, 70.
- [30] F. Pan, S. M. Chen, Y. Li, Z. Tao, J. Ye, K. Ni, H. Yu, B. Xiang, Y. Ren, F. Qin, S. H. Yu, Y. W. Zhu, *Adv. Funct. Mater.* **2018**, *28*, 1803221.
- [31] X. Li, R. J. Zhang, W. J. Yu, K. L. Wang, J. Q. Wei, D. H. Wu, A. Y. Cao, Z. H. Li, Y. Cheng, Q. S. Zheng, R. S. Ruoff, H. W. Zhu, *Sci. Rep.* **2012**, *2*, 870.
- [32] T. T. Yang, W. Wang, H. Z. Zhang, X. M. Li, J. D. Shi, Y. J. He, Q. S. Zheng, Z. H. Li, H. W. Zhu, *ACS Nano* **2015**, *9*, 10867.
- [33] X. N. Wang, Y. F. Qiu, W. W. Cao, P. A. Hu, *Chem. Mater.* **2015**, *27*, 6969.
- [34] J. Lee, S. Shin, S. Lee, J. Song, S. B. Kang, H. Han, S. G. Kim, S. Kim, J. Seo, D. E. Kim, T. Lee, *ACS Nano* **2018**, *12*, 4259.
- [35] S. Ryu, P. Lee, J. B. Chou, R. Xu, R. Zhao, A. J. Hart, S. G. Kim, *ACS Nano* **2015**, *9*, 5929.
- [36] Z. Y. Liu, D. P. Qi, G. Y. Hu, H. Wang, Y. Jiang, G. Chen, Y. F. Luo, X. J. Loh, B. Liedberg, X. D. Chen, *Adv. Mater.* **2018**, *30*, 1704229.
- [37] R. Wang, N. Jiang, J. Su, Q. Yin, Y. Zhang, Z. S. Liu, H. B. Lin, F. A. Moura, N. Y. Yuan, S. Roth, R. S. Rome, R. Ovalle-Robles, K. Inoue, S. Yin, S. L. Fang, W. C. Wang, J. N. Ding, L. Q. Shi, R. H. Baughman, Z. Liu, *Adv. Funct. Mater.* **2017**, *27*, 1702134.
- [38] S. Park, S. Ahn, J. Z. Sun, D. Bhatia, D. Choi, K. S. Yang, J. Bae, J. J. Park, *Adv. Funct. Mater.* **2019**, *29*, 1808369.
- [39] M. C. Zhang, C. Y. Wang, H. M. Wang, M. Q. Jian, X. Y. Hao, Y. Y. Zhang, *Adv. Funct. Mater.* **2017**, *27*, 1604795.
- [40] Y. Jiang, Z. Y. Liu, N. J. Matsuhisa, D. P. Qi, W. R. Leow, H. Yang, J. C. Yu, G. Chen, Y. Q. Liu, C. J. Wan, Z. J. Liu, X. D. Chen, *Adv. Mater.* **2018**, *30*, 1706589.
- [41] X. W. Wang, Y. Gu, Z. P. Xiong, Z. Cui, T. Zhang, *Adv. Mater.* **2014**, *26*, 1336.